KRONOS FUSION ENERGY

PAPER 2.43 · THE KRONOS 2026 SERIES

First-Wall Thermomechanics and Fatigue Life of Plasma-Facing Components Under Combined Surface and Volumetric Loading in a Compact Spherical-Tokamak Breeder

The plasma-facing components (PFCs) of a compact breeder live simultaneously inside a hard MeV neutron field, a cyclic surface heat load, and a demount–remate maintenance duty;...

Read it live — 3-D model · physics validator · film series

BY P I FORD AND G L KULCINSKI

2026 · EDITORIAL EDITION

THE OFFICIAL RECORD

What this document is, and how to read its numbers

This is a combined editorial. It gathers, in one volume, the two design studies Kronos Fusion Energy released in 2026 — a compact spherical-tokamak tritium/helium-3 breeder and a deuterium–helium-3 tandem-mirror generator — together with the intellectual-property estate, the people, and, in the internal edition, the full commercial case. The scientific text is the same text that appears in the arXiv preprints and the journal submissions; the editorial adds the apparatus a reader needs to hold the whole program at once, and nothing in the physics is altered to fit it.

THE HONESTY STANCE IS THE ASSET

Every headline quantity carries an **evidence class** — DERIVED RECOMPUTED MEASURED REQUIREMENT — and, where a number is a modelled extrapolation rather than a demonstrated value, it is labelled as such and its downside is shown next to it. Several quantities in the underlying corpus moved after first publication; where a value has been withdrawn or restated, the record says so plainly. This is deliberate: a diligence team will find the load-bearing assumptions, so the document surfaces them first.

TWO EDITIONS

This volume is issued in two editions. The **public edition** (light) carries the physics and the design only — no dollar, price, or per-kilogram figure appears anywhere in it. The **internal edition** (dark) adds the economics, the funding architecture, and the defense-commercial analysis, and is marked *Confidential* accordingly; it is not for public distribution. Where the commercial case rests on a modelled assumption rather than a demonstrated one, it is labelled as such and its downside is shown alongside it, on the same terms as the physics.

TITLE	The Kronos Fleet — Hyperion · Aegis · MetroVolt: A Combined Design & Commercialization Study
AUTHOR	Priyanca Ford, Founder & CEO, on behalf of Kronos Fusion Energy
EDITION	2026 Combined Editorial · first issue
COMPANION WORKS	The five-paper arXiv drop — (1) Breeder, (2) Burner, (3) REBCO magnet & tape, (4) Direct Energy Conversion, (5) AI/ML/Quantum control — with matching numbered Zenodo deposits, plus the IOP journal and IAEA-FEC submissions. Patents were filed before the drop.
NAMING	Hyperion = the breeder; Aegis (defense) and MetroVolt (data-center) = one generator in two housings. Internal mode letters (D1, L) do not appear on public surfaces.
STATUS	Conceptual design & simulation study. Nothing herein is a construction commitment.

HOW TO READ THIS VOLUME

The fleet at a glance, and the way its numbers are marked

This volume opens with *Orientation*, presents the five research papers as a bound sequence, and closes with the *Apparatus*. *Foundations* sets out the three general results both machines rest on. *Paper One* is the Hyperion breeder; *Paper Two* the Aegis / MetroVolt generator; *Papers Three, Four and Five* are the enabling science — high-field REBCO magnets and tape, direct energy conversion, and the AI / ML / quantum control stack. A *Digital Twin & 3-D Model* part follows, then the *Environmental* profile. The *Economics* and levelized cost and the *Business Case* and diligence record appear in the internal edition only; the *Simulations* proof record and the Apparatus — patent portfolio, team, limitations, and sources — close both editions.

THE FLEET AT A GLANCE

	HYPERION	AEGIS	METROVOLT
Role	Strategic-isotope foundry	Defense installation power	Campus power
Machine	**Spherical tokamak**	**Tandem mirror**	**Tandem mirror**
Fuel	Deuterium–tritium	Deuterium–helium-3	Deuterium–helium-3
Delivers	Tritium · ^{3}He · 14 MeV n	Resilient installation power	Firm campus power
Physics bar	**Fusion gain only**	Closure (gates named)	Closure + lunar ^{3}He
In the fleet	Breeds the fuel	Proves the generator	Commercial destination

HOW THE NUMBERS ARE MARKED

Every headline quantity carries an evidence class — DERIVED from first principles, RECOMPUTED from raw data, MEASURED in hardware, or a REQUIREMENT yet to be met. Financial figures carry a case label and are confined to the internal (confidential) edition. Values that moved after first publication are shown as withdrawn or restated rather than quietly changed. A capability you can evaluate is one whose limits are on the page.

ABSTRACT

First-Wall Thermomechanics and Fatigue Life of Plasma-Facing Components Under Combined Surface and Volumetric Loading in a Compact Spherical-Tokamak Breeder

The plasma-facing components (PFCs) of a compact breeder live simultaneously inside a hard 14 MeV neutron field, a cyclic surface heat load, and a demount–remate maintenance duty; the engineering question is not *whether* the wall is loaded but *which* mechanism sets its life. We pose the coupled thermomechanical, radiation-damage and fatigue problem for the Hyperion breeder at its frozen design point ($P_{\text{fus}} = 85.04$ MW, $I_p = 9.66$ MA, $Q = 3.076$, negative triangularity $\delta = -0.30$, first-wall neutron loading $\Gamma_{\text{w}} = 1.885$) and solve each failure mode from its governing equations. We write the conjugate heat-transfer problem with a combined Neumann surface flux and a volumetric nuclear source and a Robin coolant condition; the thermoelastic stress from constrained thermal expansion; the Norgett–Robinson–Torrens (NRT) and athermal-recombination-corrected displacement model folded against the primary-knock-on spectrum; helium-bubble rate theory closed by a van der Waals equation of state; and the Coffin–Manson–Basquin strain–life law with Palmgren–Miner accumulation. Solved on the NVIDIA GPU high-performance-computing (HPC) campaign with OpenMC/DAGMC transport-and-depletion, LAMMPS molecular-dynamics cascades, RustBCA binary-collision sputtering, and a finite-element conjugate-heat-transfer solver, the results are unambiguous. Every mechanical and materials mode carries margin: tungsten plasma-facing swelling is $0.024\,\%$ per full-power year (fpy) and reduced-activation ferritic–martensitic (RAFM) swelling $0.017\,\%$/fpy against a 1–$5\,\%$ tolerance; the cumulative Palmgren–Miner fatigue damage from pulsed operation is 3×10^{-6}; the demountable-joint fatigue life is 1.09×10^{6} cycles, $5434\times$ the 200-mate design duty; the self-cooled lithium first wall runs at a RAFM structural temperature of 516 with a 34 margin, contingent on a ≤ 6 mm channel depth. What binds is bulk neutron displacement damage: the wall accumulates 18.85 , which sets a *scheduled-replacement cadence* rather than a thermomechanical failure. The lifetime case is therefore clean and legible — fatigue and swelling sit orders of magnitude inside their limits — and the single design driver is a plannable, damage-limited replacement interval sized by a first-principles calculation.

Open-access deposit (code & data, CC BY 4.0): DOI 10.5281/zenodo.22645850 · Zenodo community *kronos_fusion_energy*. Explore it live: interactive 3-D model · physics validator.

Keywords: first-wall thermomechanics · thermal stress · fatigue · Miner damage · NRT dpa · helium swelling · sputter erosion · plasma-facing-component lifetime · spherical-tokamak breeder

CONTENTS

Table of Contents

NOMENCLATURE

Symbols, units, and the names of things

Q	plasma (fusion) gain, P_{fus}/P_{aux}
Q_E	engineering gain, net electric out / recirculating in
H_{98}	confinement enhancement over the IPB98(y,2) scaling
Z_{eff}	effective ion charge
c_{ee}	electron–electron bremsstrahlung leading coefficient, 2.120022 (exact)
τ_E	energy confinement time
I_p	plasma current
R_0, a	major radius, minor radius
κ, δ	elongation, triangularity
β_N	normalized plasma beta (Troyon-normalized)
TBR	tritium breeding ratio
DEC	direct energy conversion
CF	plant capacity factor (availability)
FOAK / NOAK / BOAK	first / n^{th} / best of a kind
Hyperion	the ST breeder (internal: Mode D2)
Aegis	the generator, defense/installation housing (internal: Mode M)
MetroVolt	the generator, data-center housing (Mode M)

§ 1

Introduction

WHY THE COMPACT-ST FIRST WALL IS THE INTERESTING CASE

A spherical tokamak (ST) confines a large plasma current in a small volume, which is exactly what makes it an attractive compact neutron source and breeder platform [1,2], and exactly what concentrates fusion power onto a small first-wall area. At the Hyperion design point the plasma delivers $P_{\text{fus}} = 85.04$ MW with a neutron power $P_{\text{n}} = 67.79$ MW behind a centrepost magnet at a peak field of 16.84 T, in a negative-triangularity ($\delta = -0.30$) configuration [3,4]. The resulting first-wall neutron loading is $\Gamma_{\text{w}} = 1.885$, comparable to that of a demonstration power plant but pressed into the geometry of a compact device. The plasma-facing components therefore see three loads at once: a *surface* heat flux from charged-particle transport and radiation, a *volumetric* nuclear heating and displacement source from the neutron field, and a *cyclic* mechanical and thermal duty from pulsed operation and from the demount–remate maintenance concept of a machine built around a consumable centrepost. The negative-triangularity edge is quiet and free of the edge-localised-mode (ELM) cycle of conventional H-mode [3,4], which keeps the transient surface loads well-behaved [34,29]; the steady, coupled loading is what remains to be answered.

The engineering question this paper settles is a comparative one: given the frozen operating point, *which* of the candidate failure modes — thermal overrun, thermal-stress ratcheting, cyclic fatigue, radiation-driven swelling, sputter erosion, or bulk displacement damage — actually sets the plasma-facing- component lifetime? We answer it by writing each mode as a governing-equations problem, solving it on the GPU high-performance-computing (HPC) campaign against the frozen anchors, and comparing the resulting margins on a single normalised scale.

PRIOR ART

The mechanics and materials science underlying each mode are individually mature. Steady-state and transient first-wall thermal-hydraulics and the associated temperature-window constraints for fusion structural materials were placed on a quantitative footing by Zinkle and Ghoniem [7], who defined operating windows bounded below by radiation embrittlement and above by thermal creep for the reduced-activation ferritic–martensitic (RAFM) steels, copper alloys and refractory metals of interest here. The reference RAFM steel EUROFER and its oxide-dispersion-strengthened variant carry a conservative $250\text{–}550$ window that directly bounds the structural design [8]. Tungsten as a plasma-facing armour, its thermophysical envelope, and its neutron-transmutation behaviour have been reviewed comprehensively [9,10]. Radiation damage is quantified through the Norgett–Robinson–Torrens (NRT) displacement standard [5], now refined by the athermal-recombination-corrected (arc-dpa) model of Nordlund *et al.* [6], which shows that the surviving defect count in an energetic cascade is only about one third of the NRT value — a correction we carry explicitly. Helium accumulation and bubble-driven swelling, the materials mode most feared at high displacement dose, were framed by Trinkaus and Singh [11] and set in the broader radiation-resistance context by Zinkle and Snead [12] and Odette *et al.* [13]. Sputter erosion and the wider plasma–material-interaction picture are reviewed by Federici *et al.* [14], with the physical-sputtering yield captured by the Bohdansky formula [15]. Low-cycle fatigue rests on the Coffin–Manson strain–life law and the Palmgren–Miner linear-damage rule [16].

What the literature does not supply is an *integrated*, frozen-design-point answer for a compact ST breeder: a single calculation that (i) states each mode as a governing-equations problem at one operating point, (ii) solves it with production nuclear- and materials-physics codes on a common GPU campaign, and (iii) places the resulting margins on one comparable scale so that the binding constraint is identified rather than asserted. This paper contributes exactly that. It sits alongside the companion neutron-damage-lifetime study [28] and plasma–material-interaction study [29], the blanket and divertor thermal-hydraulics paper [30], the RAFM-qualification paper [31], and the centrepost fluence-and-shielding [32] and remaining-useful-life [33] papers, to which the reader is referred for the modes treated in depth elsewhere.

CONTRIBUTION

We (i) pose the coupled surface-plus-volumetric conjugate-heat-transfer and thermoelastic problem for the first wall and reduce it to a solvable one-dimensional heat-path model calibrated to the two-dimensional frozen result (§2); (ii) write the displacement-damage source from the NRT/arc-dpa model folded against the molecular-dynamics primary-knock-on spectrum, and the helium-swelling rate-theory closed by a van der Waals bubble equation of state (§2); (iii) state the fatigue and erosion laws and the formal lifetime-minimisation problem that selects the binding mode (§2); (iv) describe the numerical formulation and the NVIDIA GPU HPC campaign that produced every number (§3); (v) report the solved margins with nine figures and three tables (§4); and (vi) benchmark the results against the published thermomechanics, damage and swelling literature (§5). Every quantitative claim traces to a frozen result in the Kronos Physics De-Risking Register [27] through the serial identifiers (e.g. BR-L1-A13) cited inline, so each number is auditable.

§ 2

Governing equations and the formal problem

COMBINED SURFACE AND VOLUMETRIC LOADING

Let $\Omega \subset \mathbb{R}^3$ be the plasma-facing-component domain with plasma-facing surface Γ_p and coolant surface Γ_c (figure 1). The wall is loaded by a surface heat flux q'' deposited on Γ_p and a volumetric nuclear heating density $q'''(r)$ deposited throughout Ω by the neutron and secondary-gamma field. The volumetric source scales with the wall neutron loading; writing $\mu(r)$ for the local nuclear-heating response,

$$q'''(r) = \mu(r)\,\Gamma_\mathrm{w}, \qquad \Gamma_\mathrm{w} = 1.885 \quad \mathrm{MW\,m^{-2}},$$

so that the same neutron current that heats the wall also displaces its atoms and breeds its transmutant gas (§2.4–§2.5). This coupling — one field driving heat, damage and gas together — is what makes the first-wall problem irreducibly multi-physics.

CONJUGATE HEAT TRANSFER

The temperature field $T(r,t)$ obeys the heat equation with an anisotropic, temperature-dependent conductivity $k(T, r)$,

$$\rho c_p \frac{\partial T}{\partial t} = \nabla\cdot\big(k(T, r)\,\nabla T\big) + q'''(r),$$

closed by a Neumann condition on the plasma-facing surface, a Robin (convective) condition on the coolant surface, and adiabatic side faces,

$$-k\nabla T\cdot\hat{n}\big|_{\Gamma_\mathrm{p}} = q'', \qquad -k\nabla T\cdot\hat{n}\big|_{\Gamma_\mathrm{c}} = h\big(T - T_\mathrm{cool}\big), \qquad k\nabla T\cdot\hat{n}\big|_{\Gamma_\mathrm{s}} = 0,$$

with film coefficient h and coolant temperature T_cool. For the layered first wall (tungsten armour of thickness t_W over a RAFM structure of thickness t_R) the transverse gradients dominate and equation (2) reduces at steady state to the one-dimensional two-region problem

$$\frac{\mathrm{d}}{\mathrm{d}x}\left(k_i\,\frac{\mathrm{d}T}{\mathrm{d}x}\right) + q''' = 0, \qquad i \in \{\mathrm{W}, \mathrm{R}\},$$

with continuity of T and of heat flux $k\,\mathrm{d}T/\mathrm{d}x$ at the armour–structure interface. The local conductive flux is $q(x) = q'' + q'''x$, and integrating equation (4) from the coolant face inward gives the closed-form profile

$$T(x) = T_\mathrm{cool} + \frac{q''_\mathrm{out}}{h} + \int_x^L \frac{q'' + q'''x'}{k(x')}\,\mathrm{d}x', \qquad q''_\mathrm{out} = q'' + q'''L,$$

where $L = t_\mathrm{W} + t_\mathrm{R}$ and q''_out is the total flux delivered to the coolant. The peak structural temperature $T_\mathrm{R}^\mathrm{max} = T(t_\mathrm{W})$ occurs at the armour–structure interface and must satisfy the RAFM window constraint [7,8]

$$T_\mathrm{R}^\mathrm{max} \le T_\mathrm{lim} = 550 \quad {}^\circ\mathrm{C}.$$

THERMOELASTIC STRESS

The temperature field drives thermal strain $\varepsilon^\mathrm{th} = \alpha\,(T - T_\mathrm{ref})\,I$. With σ the Cauchy stress, quasi-static mechanical equilibrium and the thermoelastic constitutive law are

$$\nabla\cdot\sigma = 0, \qquad \sigma = \mathsf{C} : \big(\varepsilon - \varepsilon^\mathrm{th}\big) = 2G\,\varepsilon + \lambda\,\mathrm{tr}(\varepsilon)\,I - \frac{E\alpha(T - T_\mathrm{ref})}{1 - 2\nu}\,I,$$

with Lam\'e parameters (λ, G), Young's modulus E and Poisson's ratio ν. For a thin wall whose in-plane expansion is constrained by the cooler bulk, the through-thickness temperature excursion $T(x) - \bar{T}$ (with $\bar{T}$ the wall-averaged temperature) generates the biaxial thermal stress

$$\sigma_\mathrm{th}(x) = -\frac{E\alpha}{1-\nu}\big(T(x) - \bar{T}\big), \qquad \Delta\sigma_\mathrm{th} = \frac{E\alpha}{1-\nu}\,\Delta T,$$

so the peak thermal-stress range $\Delta\sigma_{\text{th}}$ is set by the through-thickness temperature drop ΔT. Equation (8) is the bridge from the thermal solution to the fatigue driver of §2.6: the per-pulse mechanical strain range is $\Delta\varepsilon = \Delta\sigma_{\text{th}}/E = \alpha\,\Delta T/(1-\nu)$.

DISPLACEMENT DAMAGE: NRT AND ARC-DPA

A 14 MeV neutron transfers energy to a lattice atom, creating a primary knock-on atom (PKA) of recoil energy T_{r} that initiates a displacement cascade. The number of stable Frenkel pairs produced is given by the Norgett–Robinson–Torrens standard [5]

$$\nu_{\text{NRT}}(T_{\text{dam}}) = \begin{cases} 0, & T_{\text{dam}} < E_d, \\ 1, & E_d \le T_{\text{dam}} < \dfrac{2E_d}{0.8}, \\ \dfrac{0.8\,T_{\text{dam}}}{2E_d}, & T_{\text{dam}} \ge \dfrac{2E_d}{0.8}, \end{cases}$$

where E_d is the effective displacement threshold and $T_{\text{dam}} = T_{\text{r}} - \bar{Q}(T_{\text{r}})$ is the damage energy remaining after electronic losses (Lindhard partition). The displacement rate per atom is the neutron flux folded with the displacement cross-section,

$$R_{\text{dpa}} = \int_0^\infty \phi(E)\,\sigma_{\text{dpa}}(E)\,\mathrm{d}E, \qquad \sigma_{\text{dpa}}(E) = \int \nu_{\text{NRT}}(T_{\text{dam}})\,\frac{\mathrm{d}\sigma}{\mathrm{d}T_{\text{r}}}\,\mathrm{d}T_{\text{r}}.$$

Molecular-dynamics cascades show that a large fraction of NRT pairs recombine athermally within the cascade; the arc-dpa model [6] replaces ν_{NRT} by $\nu_{\text{arc}} = \xi(T_{\text{dam}})\,\nu_{\text{NRT}}$ with a surviving-defect efficiency $\xi \approx 1/3$ at cascade energies, which we carry as the physical damage source while reporting the NRT value as the standard-referenced quantity. Anchored to the wall neutron loading, the frozen first-wall displacement rate is (BR-L1-A13)

$$R_{\text{dpa}} = 18.85 \qquad \text{dpa fpy}^{-1} \quad \text{at} \quad \Gamma_{\text{w}} = 1.885 \qquad \text{MW m}^{-2},$$

an essentially linear proportionality $R_{\text{dpa}} \simeq \kappa_{\text{dpa}}\,\Gamma_{\text{w}}$ with $\kappa_{\text{dpa}} \simeq 10$ dpa MW^{-1} m^2 fpy^{-1} that holds across the ST design box and makes displacement damage a simple function of the operating point. The damage source is anchored to the wall loading rather than to an uncollided flux scalar; the archived flux normalisation was audited and corrected without changing the wall-anchored dpa (BR-SX-02).

HELIUM TRANSMUTATION AND BUBBLE SWELLING

The same neutron field drives (n,α) transmutation, generating helium at a rate that tracks the displacement rate through a spectrum-dependent gas-to-damage ratio,

$$G_{\text{He}} = \left(\tfrac{\text{He}}{\text{dpa}}\right) R_{\text{dpa}}, \qquad G_{\text{He}} = 226 \text{ appm fpy}^{-1} \;\Rightarrow\; \left(\tfrac{\text{He}}{\text{dpa}}\right) \approx 12 \text{ appm dpa}^{-1},$$

for the tungsten plasma-facing surface (BR-L2-A26). Helium is nearly insoluble and precipitates into nanometre bubbles. In the rate-theory picture the mobile-helium concentration C_{He} evolves as

$$\frac{\mathrm{d}C_{\text{He}}}{\mathrm{d}t} = G_{\text{He}} - 2k_{\text{nuc}}C_{\text{He}}^2 - \beta_{\text{abs}}N_b r_b C_{\text{He}},$$

balancing generation against di-helium nucleation (k_{nuc}) and absorption by the existing bubble population of number density N_b and radius r_b (β_{abs} the capture efficiency). Each bubble holds m helium atoms at a pressure fixed by mechanical equilibrium with its surface tension γ and by a van der Waals equation of state,

$$P = \frac{2\gamma}{r_b}, \qquad P\,(V_b - m\,b_{\text{vdW}}) = m\,k_B T, \qquad V_b = \tfrac{4}{3}\pi r_b^3,$$

which closes the bubble radius given its helium content. The volumetric swelling is the bubble volume fraction

$$\frac{\Delta V}{V} = \frac{4}{3}\pi\,r_b^3\,N_b.$$

With the frozen steady-state microstructure ($N_b = 2.3\times10^{23}$ m^{-3}, $r_b = 0.63$ nm; BR-L2-A26) equation (15) evaluates to $\Delta V/V = 0.024\,\%$ per full-power year for the tungsten surface and $0.017\,\%$/fpy for the Fe-9Cr structure — both far below the 1–$5\,\%$ PFC tolerance. The swelling constraint is

$$\left.\frac{\Delta V}{V}\right|_{t_{\text{life}}} \le S_{\text{tol}} \in [1,5]\,\%.$$

FATIGUE: STRAIN–LIFE AND LINEAR DAMAGE

Pulsed operation and the demount–remate maintenance duty impose cyclic strain. The total strain amplitude partitions into elastic and plastic parts and follows the Coffin–Manson–Basquin law

$$\frac{\Delta\varepsilon_t}{2} = \frac{\sigma'_f}{E}\,(2N_f)^b + \varepsilon'_f\,(2N_f)^c,$$

with fatigue strength coefficient σ'_f and exponent b, and fatigue ductility coefficient ε'_f and exponent c. Inverting equation (17) gives the allowable cycles $N_f(\Delta\varepsilon_t)$ for each load class i — the pulsed thermal cycle with strain range $\Delta\varepsilon_{\text{th}} = \alpha\,\Delta T/(1-\nu)$ from equation (8), and the mechanical demount–remate cycle of the joint. Damage accumulates by the Palmgren–Miner rule [16]

$$D = \sum_i \frac{n_i}{N_{f,i}} \le 1,$$

with n_i the applied cycles of class i. The frozen results (QS-12) are a cumulative pulsed-cycling Miner damage of $D = 3 \times 10^{-6}$ and a demountable-joint fatigue life $N_f = 1.09 \times 10^6$ cycles against a 200-mate design duty — a $5434\times$ margin — so operation is not fatigue-limited and the joint's practical limit is wear and contact resistance, not fatigue.

SPUTTER EROSION

Charged-particle bombardment of the plasma-facing surface removes atoms by physical sputtering. The recession rate is the sputter yield $Y(E)$ times the ion flux Γ_{ion} converted to a thickness rate,

$$\dot{r}_{\text{ero}} = \frac{Y(E)\,\Gamma_{\text{ion}}\,M}{\rho\,N_A},$$

with atomic mass M, mass density ρ and Avogadro constant N_A. The physical-sputtering yield follows the Bohdansky threshold form [15]

$$Y(E) = Q\,s_n(\varepsilon)\left[1 - \left(\frac{E_{\text{th}}}{E}\right)^{2/3}\right]\left(1 - \frac{E_{\text{th}}}{E}\right)^2, \qquad E > E_{\text{th}},$$

with yield factor Q, nuclear stopping s_n and threshold energy E_{th}. Below E_{th} the yield vanishes; above it the yield rises steeply, so edge-energy control is the governing lever. At the nominal sub-500 eV edge the frozen tungsten recession is 0.1–0.3 mm yr^{-1} (AG-CX-27).

THE FORMAL LIFETIME PROBLEM

The plasma-facing-component lifetime is the shortest time at which any constraint is first violated,

$$t_{\text{life}} = \min\left\{t_{\text{dpa}},\ t_{\text{swell}},\ t_{\text{fatigue}},\ t_{\text{thermal}},\ t_{\text{ero}}\right\},$$

where t_{dpa} is set by the displacement-dose allowable, t_{swell} by equation (16), t_{fatigue} by $D = 1$ in equation (18), t_{thermal} is instantaneous feasibility of equation (6), and t_{ero} by the armour recession budget. The remainder of the paper evaluates each argument of equation (21); the result (§4) is that t_{dpa} is by far the smallest, so the wall is a displacement-damage-limited scheduled-replacement component and every other mode carries margin.

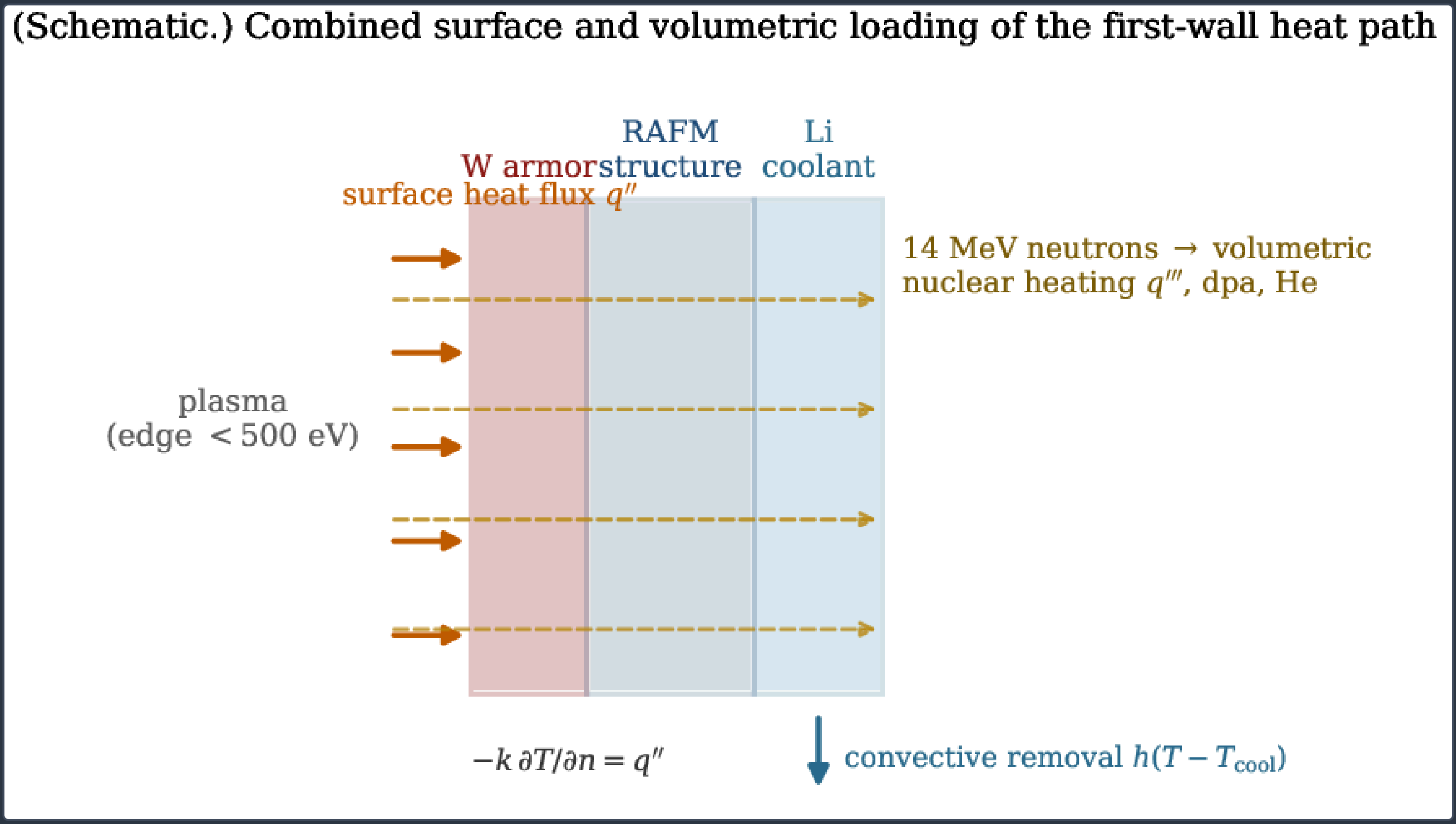

(Schematic.) Combined surface and volumetric loading of the first-wall heat path. A surface heat flux q'' enters the tungsten armour on the plasma side (Neumann condition, equation 3); the 14 MeV neutron field deposits volumetric nuclear heating q''', displacement damage and transmutant helium throughout the armour and RAFM structure (equations 1, 10, 12); the coolant removes the total flux by convection (Robin condition). No data values are shown; the figure encodes structure only.

§ 3

Computational methodology: the GPU HPC campaign

SOLVER STACK AND ROLES

Every number in this paper was produced by production nuclear- and materials-physics codes run on the NVIDIA GPU HPC campaign, each solving one of the governing problems of §2. Table 1 summarises the stack. Neutron and photon transport with full-chain depletion — the source of the volumetric heating q''', the displacement cross-section σ_{dpa}, the helium generation G_{He} and the activation inventory — is computed with OpenMC [17] on ENDF/B-VIII.0 evaluated nuclear data [18], with CAD-faithful geometry via DAGMC. The displacement-cascade source term of equation (10) is resolved from first principles by molecular-dynamics PKA cascades at 15 keV in Fe-9Cr and tungsten with LAMMPS [19], reduced to surviving-defect counts by automated Wigner–Seitz analysis and referenced to the NRT standard (BR-L2-A24). The sputter yield of equation (20) is computed by the RustBCA binary-collision-approximation code [20] (AG-CX-27, and the companion PMI study [29]). The conjugate-heat-transfer problem of equations (2)–(3) is solved by a two-dimensional finite-element solver (BR-SX-15), and the helium-bubble rate theory of equations (13)–(15) by a reduced zero-dimensional integrator corroborated by a fleet kinetic-Monte-Carlo model (BR-L2-A26).

CODE	GOVERNING PROBLEM	SERIAL
OpenMC + DAGMC [17,18]	transport/depletion: q''', σ_{dpa}, G_{He}, activation	BR-L1-A13, BV-04
LAMMPS + NRT [19]	MD PKA cascades → arc-dpa survival (eq. 10)	BR-L2-A24
RustBCA [20]	BCA sputter yield $Y(E)$ (eq. 20)	AG-CX-27
finite-element CHT	conjugate heat transfer (eqs. 2–3)	BR-SX-15
rate theory + KMC	He-bubble swelling (eqs. 13–15)	BR-L2-A26
FE structural/fatigue	thermoelastic stress and strain–life (eqs. 7, 17)	QS-12

The solver stack of the GPU HPC campaign and the governing problem each code solves. Serial identifiers refer to the Kronos Physics De-Risking Register [27].

GPU ACCELERATION AND PROBLEM SCALE

The campaign exploits GPU acceleration where each solver admits it. The Monte-Carlo transport uses GPU-resident, event-based particle tracking so that the 10^8–10^9 histories required to converge the first-wall damage-energy and heating tallies to sub-percent statistical error complete within a single allocation; the depletion chains are integrated on the same fleet. The molecular-dynamics cascades run on the GPU-accelerated (Kokkos) build of LAMMPS, with multi-million-atom simulation cells large enough to contain a 15 keV cascade and its recombination volume without periodic-image self-interaction, executed as detached multi-rank ensembles to sample the PKA spectrum. The binary-collision sputter matrix and the rate-theory and finite-element solvers are lighter and run on the same nodes. The heavy first-principles work is carried on the NVIDIA GPU fleet (A100/H100/A10 class), the same campaign that produced the negative-triangularity nonlinear gyrokinetics of the confinement paper [34]; no cost or budget figures are reported here or elsewhere in this paper.

NUMERICAL FORMULATION AND CONVERGENCE

The conjugate-heat-transfer problem is discretised by the Galerkin finite-element method. Multiplying equation (2) at steady state by a test function $w \in H^1(\Omega)$ and integrating by parts gives the weak form

$$\int_\Omega \nabla w \cdot \quad k \nabla T \,\mathrm{d}V + \int_{\Gamma_\mathrm{c}} w\, h\, T \,\mathrm{d}S = \int_\Omega w\, q''' \,\mathrm{d}V - \int_{\Gamma_\mathrm{p}} w\, q'' \,\mathrm{d}S + \int_{\Gamma_\mathrm{c}} w\, h\, T_\mathrm{cool} \,\mathrm{d}S,$$

which, with the interpolation $T \approx \sum_j T_j \varphi_j$, yields the linear system $(\quad K + \quad H) \quad T = \quad f$ where K is the conductivity stiffness, H the convective boundary matrix and f the combined surface-plus-volumetric load vector. Temperature dependence of $k(T)$ is resolved by Picard iteration to a relative residual $\| \quad r\| / \| \quad f\| < 10^{-6}$. Mesh convergence is established by uniform refinement until the peak structural temperature $T_\mathrm{R}^\mathrm{max}$ changes by less than 0.5 between successive levels; the reported profile (figure 3) is the converged solution. The structural/thermoelastic problem of equation (7) is solved on the same mesh, and the strain ranges feed equation (17). For the damage source, the MD cascades are integrated with a velocity-Verlet scheme under an adaptive timestep bounded by the fastest recoil, and the surviving Frenkel pairs are extracted by Wigner–Seitz cell occupancy once the cascade has cooled to thermal equilibrium; the NRT reference counts at 15 keV are 108.8 (Fe-9Cr) and 52.7 (W), against which the MD survival efficiency ξ is measured.

VERIFICATION AND REPRODUCIBILITY

The design point is reproduced end-to-end before any lifetime number is computed: the zero-dimensional anchor returns $Q = 3.076$, $P_\mathrm{fus} = 85.04$ MW, $I_p = 9.66$ MA and 18.85 (BR-L1-A13), and the displacement rate is confirmed against the wall-loading anchor rather than the audited flux scalar (BR-SX-02). The transport tallies are converged in the statistical sense above; the MD survival is corroborated by the independent arc-dpa literature efficiency [6]; the swelling is corroborated by an independent kinetic-Monte-Carlo model (two methods agreeing on nanometre bubbles and sub-percent swelling, BR-L2-A26). The figure-generation script and the frozen inputs are archived with the deposit (§7).

§ 4

Results

DISPLACEMENT DAMAGE SETS THE REPLACEMENT CADENCE

The first wall accumulates **18.85** at $\Gamma_w = 1.885$ (equation 11; BR-L1-A13), with a co-produced **226** appm of helium per full-power year (equation 12). Figure 2 shows the linear accumulation against an illustrative RAFM design allowable: the wall reaches a replacement threshold on a timescale of order one full-power year, fixing it as a *scheduled-replacement* component. This is the same cartridge logic that governs the inboard centrepost (§4.5), and it is the smallest argument of the lifetime minimisation (21).

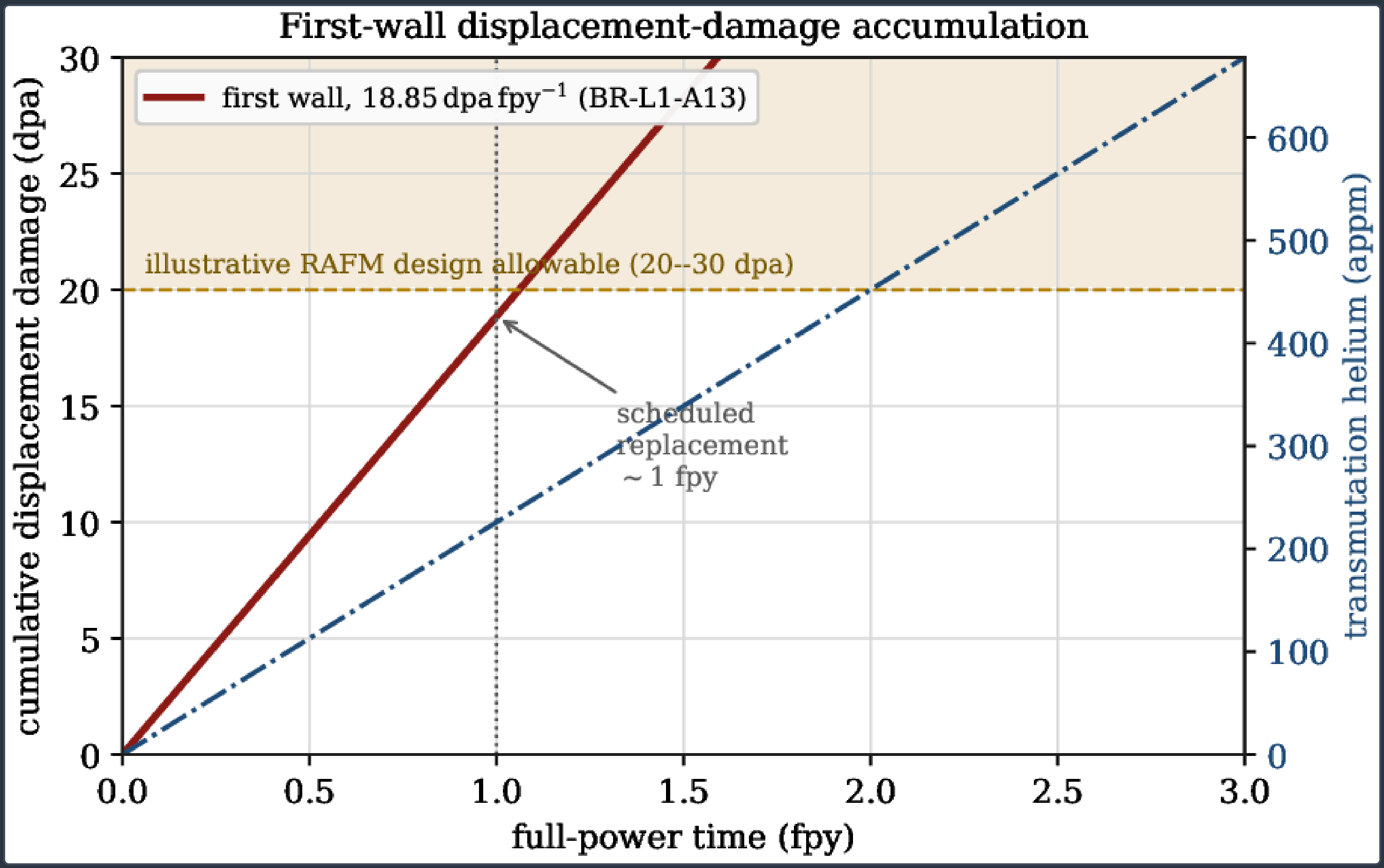

First-wall displacement-damage accumulation at $\Gamma_w = 1.885$ (**18.85** ; BR-L1-A13, equation 11), with the co-produced transmutation helium on the right axis (**226** appm/fpy; BR-L2-A26). The wall is a scheduled-replacement component set by displacement damage; the dashed band is an illustrative RAFM design allowable.

THERMOMECHANICS OF THE HEAT PATH

Solving the conjugate-heat-transfer problem of equations (2)–(5) for the self-cooled lithium first wall gives the through-thickness temperature profile of figure 3. The peak RAFM structural temperature is **516** at the armour–structure interface — a **34** margin to the **550** limit of equation (6) — provided the first-wall coolant channel is held to $\leq$ **6** mm depth at $\leq$ **15** mm pitch (BR-SX-15). The implied lithium coolant temperature from equation (5) is $\approx$ **409** , comfortably inside the RAFM window. A helium-cooled HCPB configuration, by contrast, overruns to **712** as configured and is rejected; figure 3 shows the coolant down-select as the peak structural temperature versus channel depth for the two coolants against the **550** limit. The thermal design therefore selects the coolant and the channel geometry, and the structure then runs with margin. The divertor, a distinct component, is copper-alloy (CuCrZr) limited with a coolable surface-flux capability of order **5–10** (BR-SX-15); keeping the divertor inside that band is a requirement carried by the edge and exhaust control [30] and is not a first-wall constraint.

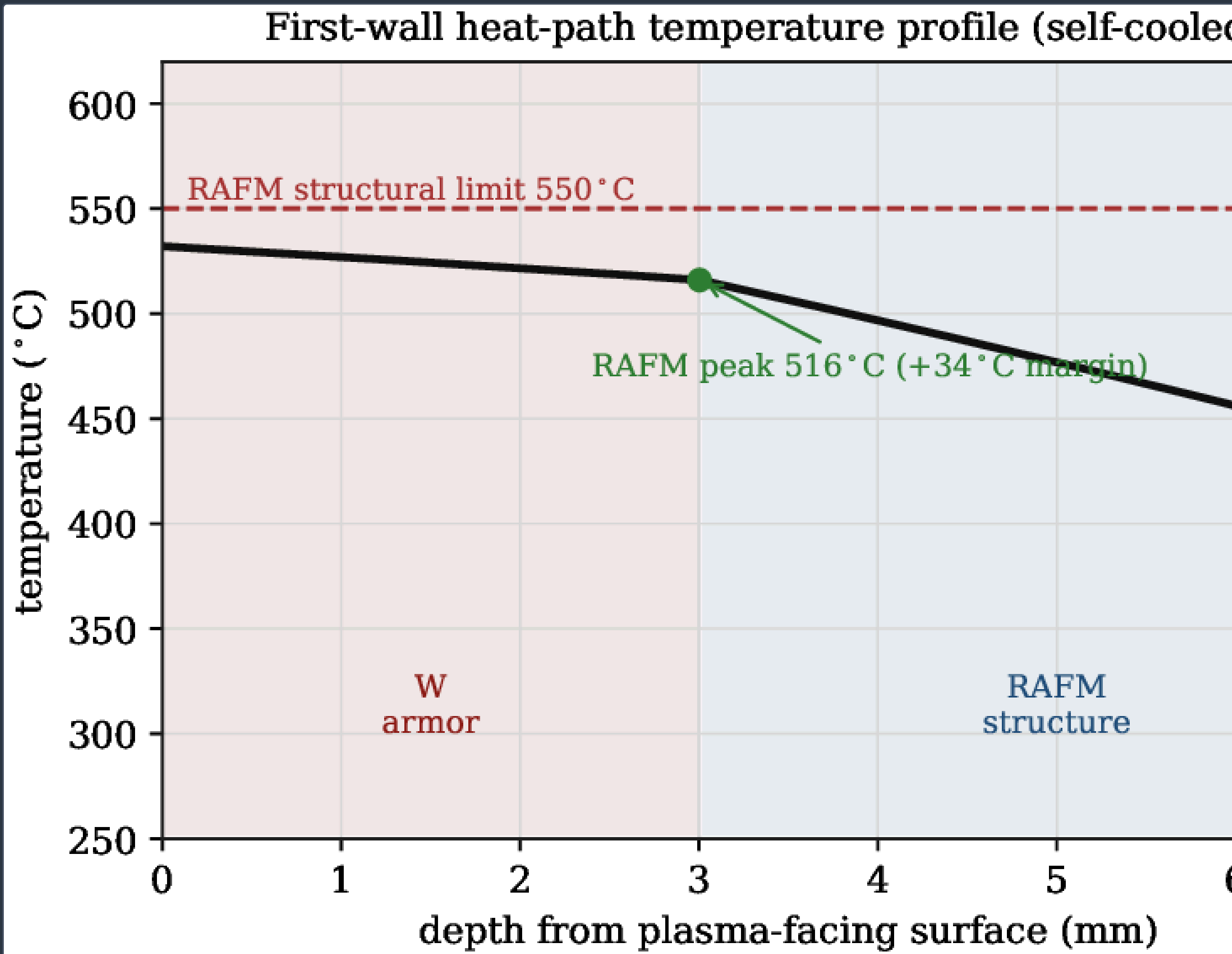
First-wall heat-path temperature profile (self-cooled
RAFM structural limit 550 °C
RAFM peak 516 °C (+34 °C margin)
W
armor
RAFM
structure
temperature (°C)
depth from plasma-facing surface (mm)
600
550
500
450
400
350
300
250
0
1
2
3
4
5

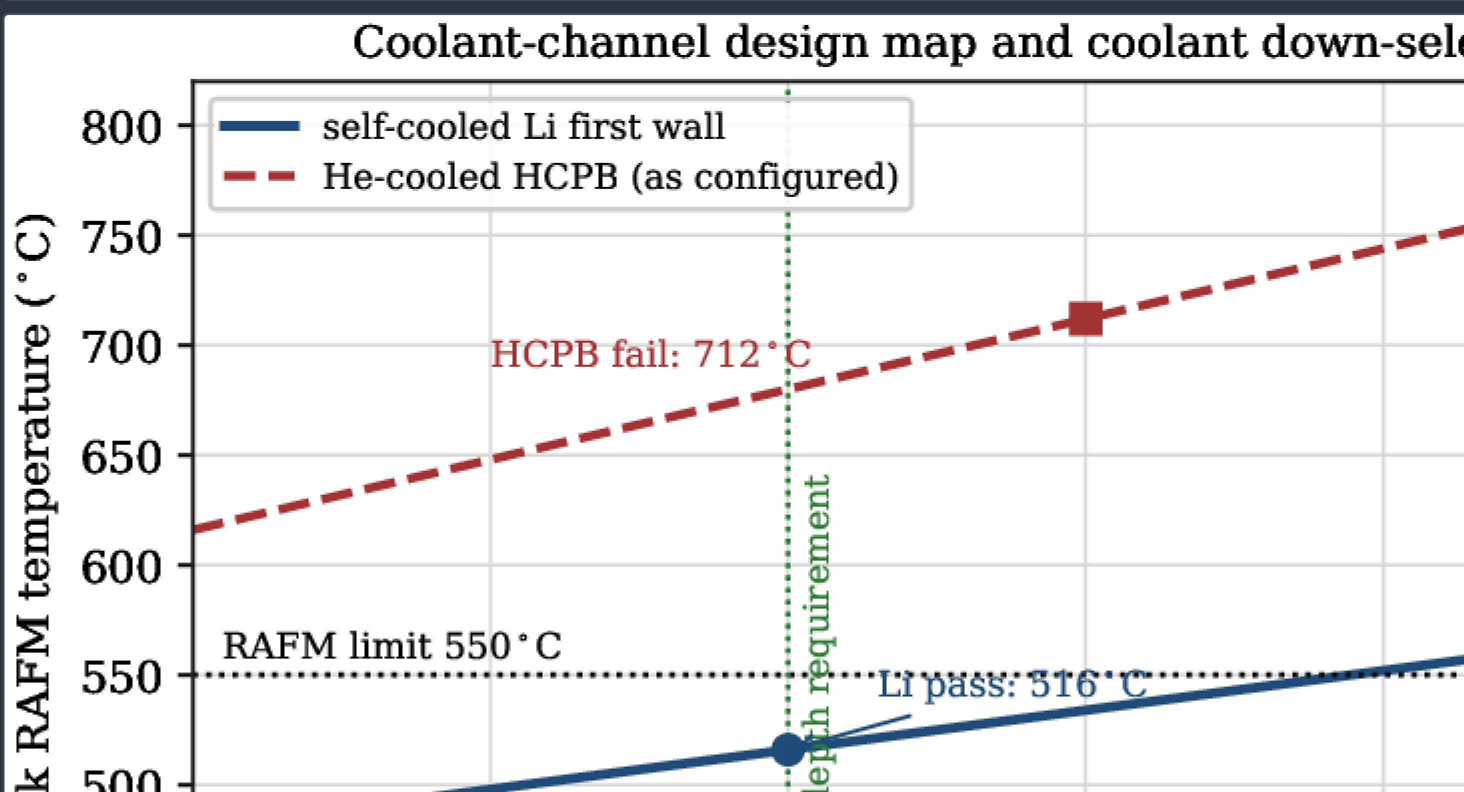
Coolant-channel design map and coolant down-sele
self-cooled Li first wall
He-cooled HCPB (as configured)
HCPB fail: 712 °C
RAFM limit 550 °C
Li pass: 516 °C
depth requirement
800
750
700
650
600
550
500

FATIGUE UNDER PULSED OPERATION AND THE DEMOUNT DUTY

The cyclic strain from pulsed thermal cycling and from the demount–remate maintenance duty is evaluated through equations (17)–(18). Figure 4 places the two load classes on the RAFM strain–life curve. The cumulative Palmgren–Miner damage from pulsed thermal cycling is $D = 3 \times 10^{-6}$ — twelve orders below the unity failure criterion — so operation is not fatigue-limited. The demountable magnet joint, the most-cycled structural interface, has a fatigue life of $N_f = 1.09 \times 10^6$ cycles, $5434\times$ the 200-mate design duty (QS-12), so its practical limit is set by wear and contact resistance rather than by fatigue. Fatigue is by a wide margin the least binding argument of equation (21).

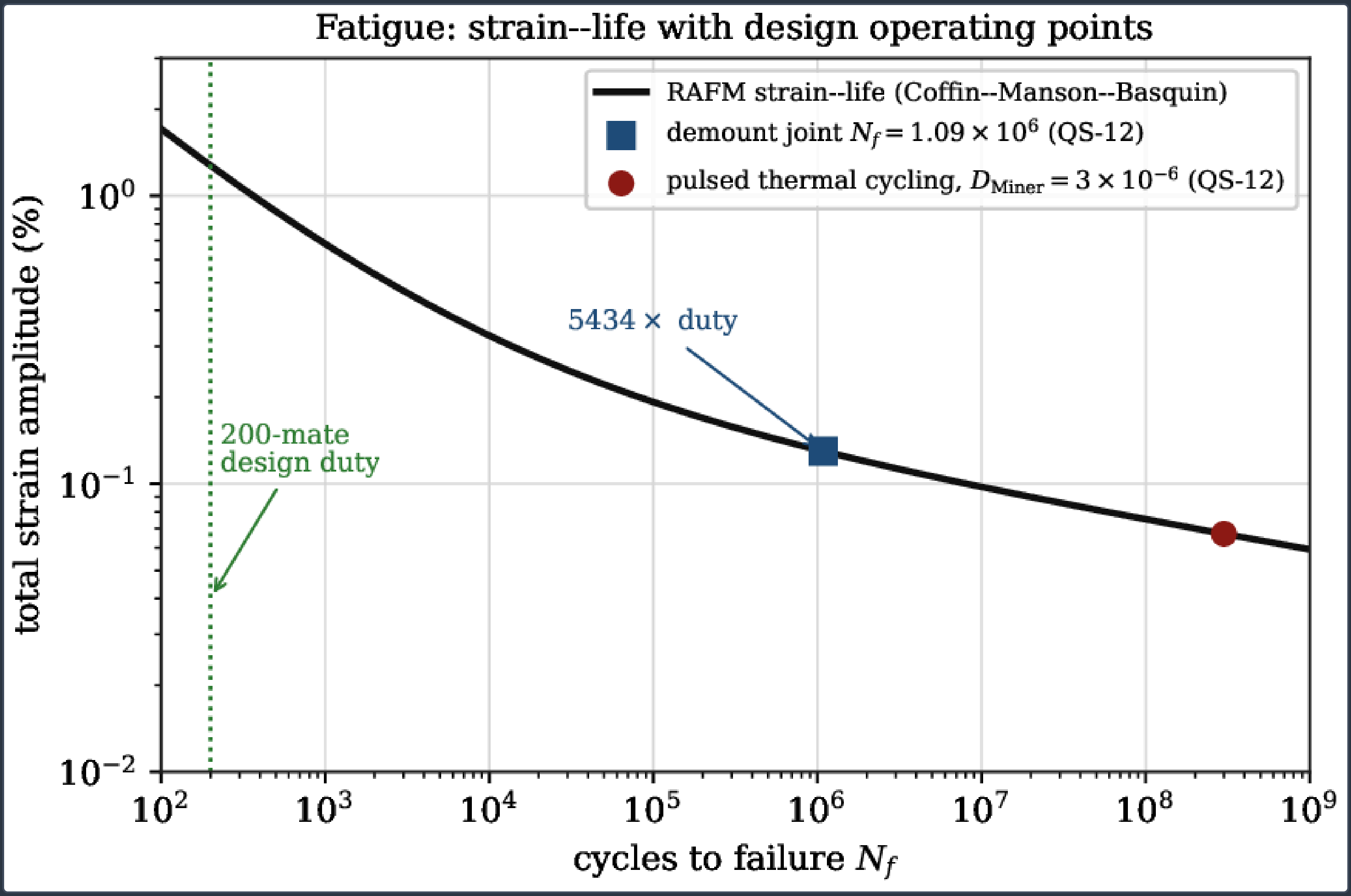

Fatigue strain–life (Coffin–Manson–Basquin, equation 17) for the RAFM structure, with the two design load classes marked (QS-12): the pulsed thermal cycle with cumulative Miner damage $D = 3 \times 10^{-6}$, and the demountable joint with $N_f = 1.09 \times 10^6$ cycles against the 200-mate design duty ($5434\times$ margin).

SWELLING AND EROSION

Radiation-driven swelling, evaluated from the bubble rate theory of equations (13)–(15) with the frozen microstructure, is small: $0.024\,\%$/fpy for the tungsten plasma-facing surface and $0.017\,\%$/fpy for the Fe-9Cr structure (figure 5), both far below the 1–$5\,\%$ tolerance of equation (16) and corroborated by the independent kinetic-Monte-Carlo model (BR-L2-A26). Even at ten full-power years the tungsten surface reaches only $0.24\,\%$, still a factor of four inside the conservative lower bound. Sputter erosion of the tungsten surface, from equations (19)–(20), is 0.1–0.3 mm yr^{-1} at the nominal sub-500 eV edge (figure 5; AG-CX-27), steep only above the Bohdansky threshold, so edge-energy control keeps it manageable. On the back end, the replaced first wall is fixed to Class-C waste by holding niobium below 5 wppm, with component-resolved shutdown-dose and decay-heat source terms established by depletion (BV-04) [35] — a materials choice, made at the composition level, that keeps the waste stream manageable.

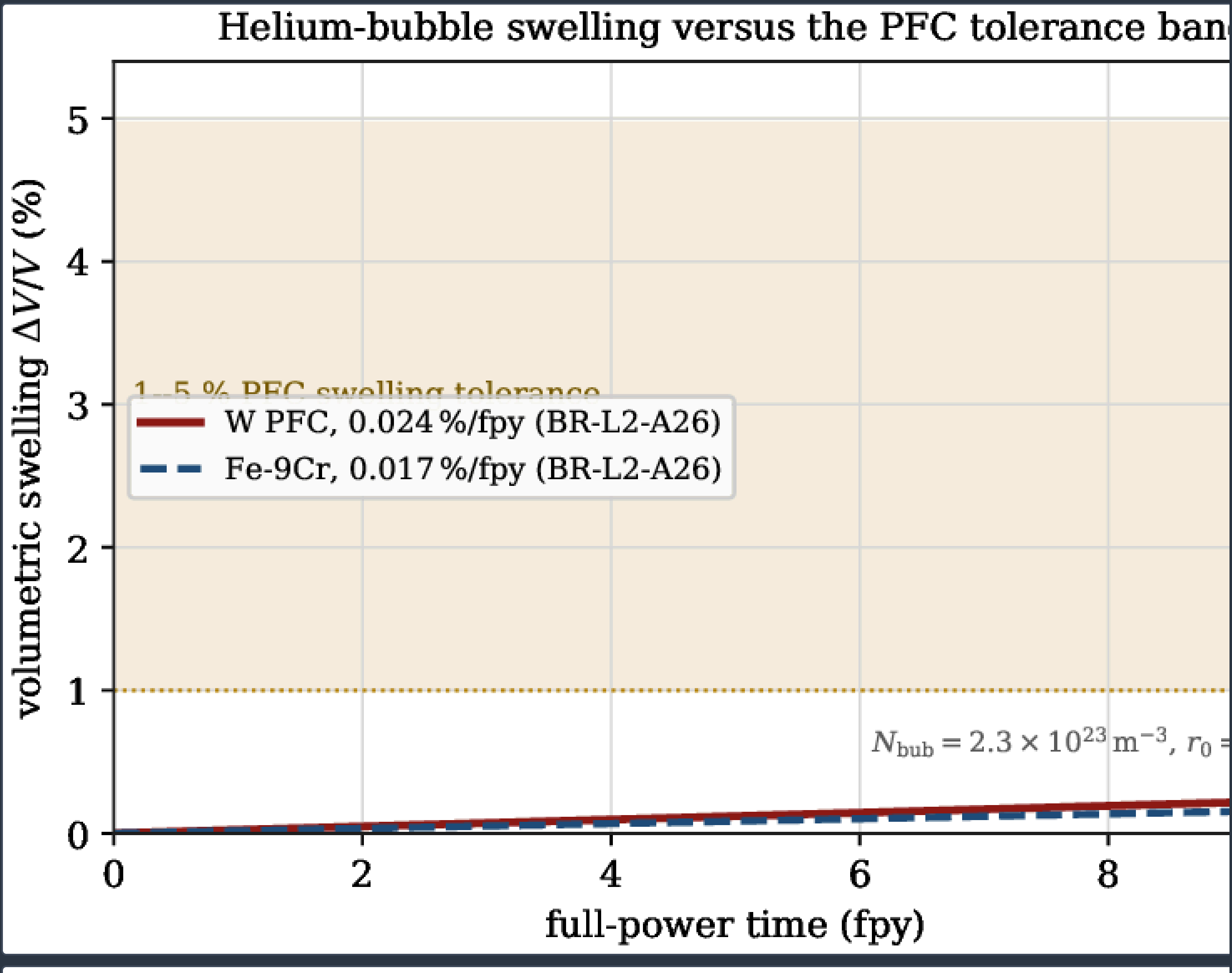
Helium-bubble swelling versus the PFC tolerance ban
volumetric swelling ΔV/V (%)
full-power time (fpy)
1--5 % PFC swelling tolerance
W PFC, 0.024 %/fpy (BR-L2-A26)
Fe-9Cr, 0.017 %/fpy (BR-L2-A26)
$N_{bub} = 2.3 \times 10^{23}$ m^{-3}, r_0 =
0
1
2
3
4
5
0
2
4
6
8

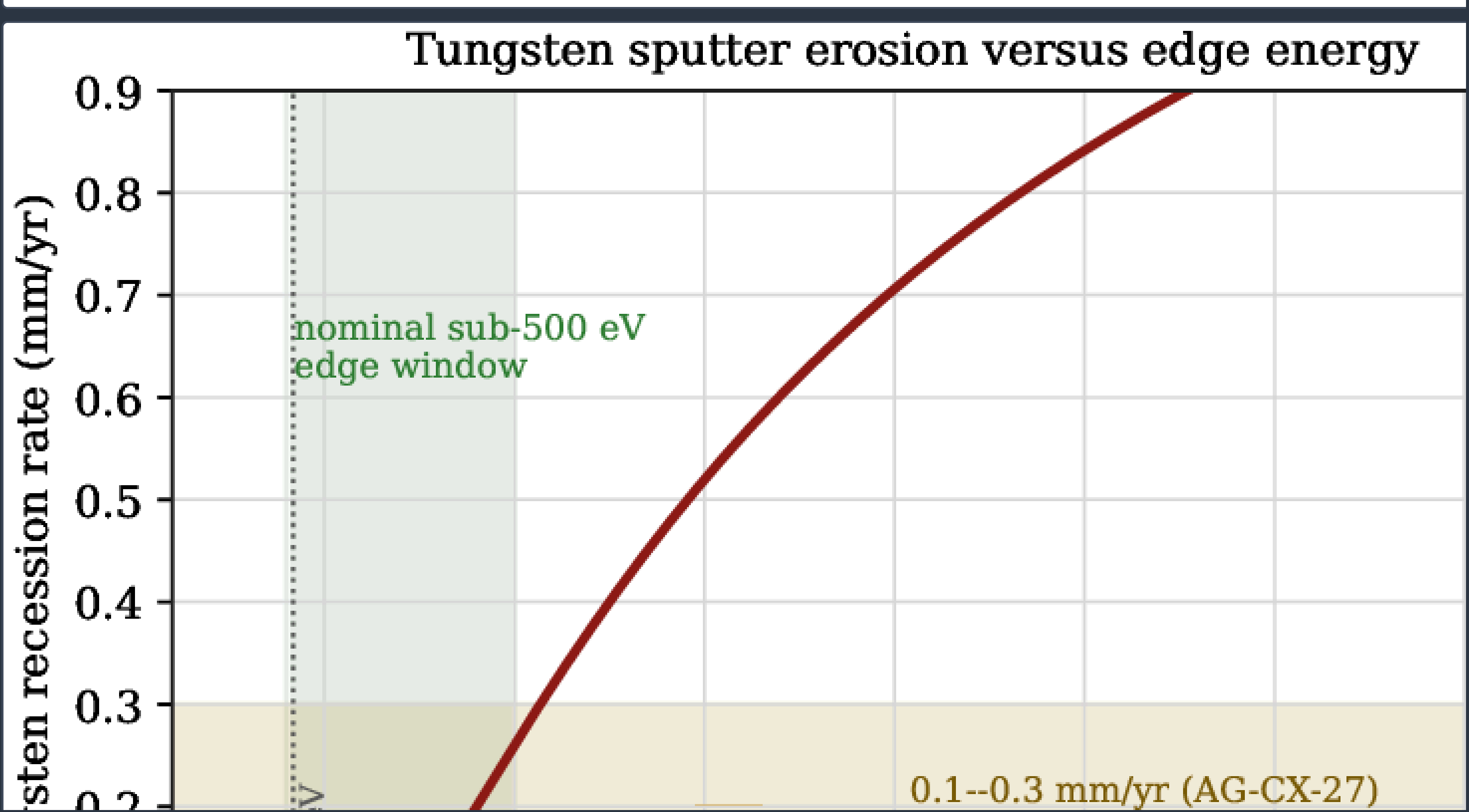
Tungsten sputter erosion versus edge energy
sten recession rate (mm/yr)
nominal sub-500 eV
edge window
0.1--0.3 mm/yr (AG-CX-27)
0.3
0.4
0.5
0.6
0.7
0.8
0.9

THE CENTREPOST TRADE

The inboard centrepost shares the wall's displacement-limited character but at a far harder fluence, and it is protected by an inboard shield rather than replaced with the first wall. Figure 6 shows the frozen life-versus-shield trade (BR-L1-A13b): as the inboard tungsten-carbide shield grows from 0 to 45 cm the fast neutron fluence ($E > 0.1$ MeV) falls from 2.9×10^{25} to 1.7×10^{23} $\mathrm{n\,m^{-2}}$ per full-power year, and the centrepost life extends from 0.003 to 0.58 fpy, approaching a $\sim$one-fpy swap cadence. The centrepost is thus a demountable, scheduled-replacement cartridge that breeds from the outboard side; it is treated in full in the centrepost fluence-and-shielding [32] and remaining-useful-life [33] papers of this series. The two magnets of the platform — the breeder centrepost at 16.84 T and the separate burner plug coil — are distinct devices and are never conflated; only the breeder centrepost is relevant here.

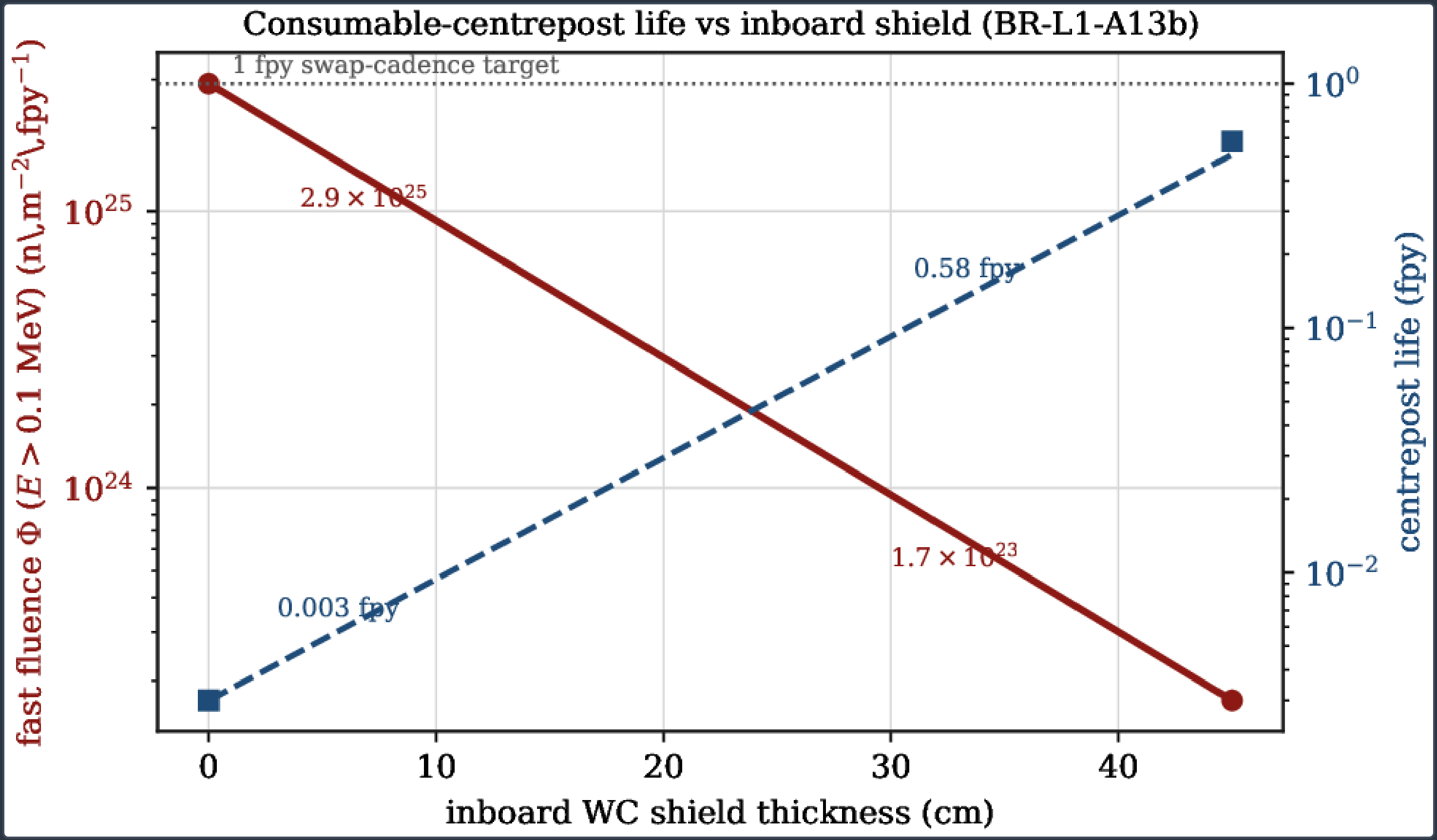

Consumable-centrepost life (right axis) and fast neutron fluence ($E > 0.1$ MeV, left axis) versus inboard WC shield thickness (BR-L1-A13b). Markers are the frozen anchors; the curves are the attenuation and fluence-limited-life models. A 45 cm shield buys a life approaching the one-fpy swap cadence.

MARGIN SYNTHESIS

Table 2 collects the solved margins, and figure 7 normalises each mode to its allowable limit on a single logarithmic scale. The picture is unambiguous: fatigue sits twelve orders inside its limit; swelling a factor 40–60 inside; erosion a factor of ten inside its recession budget; the RAFM structural temperature is the tightest of the thermomechanical modes at 94 % of its limit yet still with a 34 margin; and bulk displacement damage is the binding constraint that defines the replacement cadence. Every argument of the lifetime minimisation (21) except t_{dpa} carries comfortable margin.

MECHANISM	VALUE	LIMIT / CRITERION	SERIAL
He-bubble swelling (W PFC)	0.024 %/fpy	1–5 % tolerance	BR-L2-A26
He-bubble swelling (Fe-9Cr)	0.017 %/fpy	1–5 % tolerance	BR-L2-A26
cyclic fatigue (Miner sum)	3×10^{-6}	< 1	QS-12
demount-joint fatigue life	1.09×10^{6} cyc	5434× the 200-mate duty	QS-12
RAFM structural temperature	516	34 margin to 550	BR-SX-15
W sputter erosion	0.1–0.3 mm/yr	sub-500 eV edge	AG-CX-27
first-wall neutron damage	18.85	scheduled replacement (binding)	BR-L1-A13

Plasma-facing-component lifetime margins at the frozen design point. Every mechanical and materials mode carries margin; bulk displacement damage sets the scheduled-replacement cadence. Serials refer to the register [27].

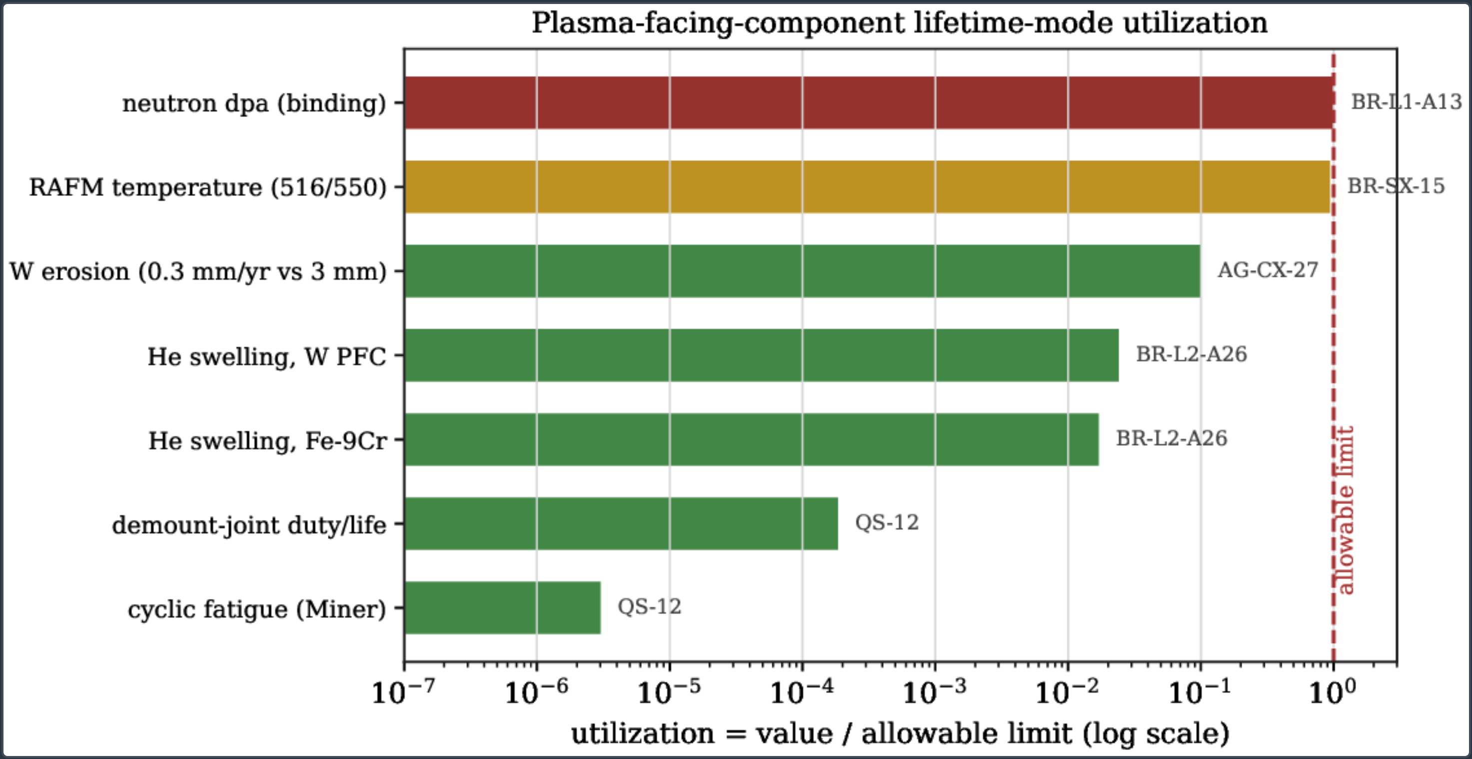

Lifetime-mode utilisation normalised to the allowable limit for each mode (log scale). Helium swelling, cyclic fatigue, erosion and structural temperature all sit inside their limits; the binding constraint is bulk neutron displacement damage, treated as a scheduled-replacement cadence (Table 2).

§ 5

Discussion

AGAINST THE PUBLISHED THERMOMECHANICS AND MATERIALS BENCHMARKS

The results place the compact-ST first wall squarely inside the envelope established by the fusion-materials literature. The 516 structural temperature against a 550 RAFM limit is exactly the upper bound of the conservative EUROFER operating window reported by Lindau *et al.* [8] and by the operating-temperature-window analysis of Zinkle and Ghoniem [7]; the 34 margin is thin by design, and it is the thermal solution — not any radiation-damage mode — that would tighten first if the surface load rose, which is why the coolant and channel geometry are treated as the primary thermal design variables (figure 3). The helium-to-damage ratio of $\approx 12\,\mathrm{appm\,dpa}^{-1}$ (equation 12) is characteristic of a first-wall 14 MeV spectrum and consistent with the transmutation behaviour reviewed for tungsten by Gilbert and Sublet [10]; the resulting sub-percent swelling is well below the levels at which helium embrittlement and bubble-driven swelling become design-limiting in the analyses of Trinkaus and Singh [11] and Zinkle and Snead [12]. The finding that displacement damage — not swelling, fatigue or thermal margin — is the binding constraint matches the broad conclusion of the structural-materials community that neutron dose, expressed in dpa, is the fundamental life-limiter for fusion structures [12,13].

THE ARC-DPA CORRECTION AND WHY THE CADENCE IS ROBUST

Carrying the arc-dpa efficiency $\xi \approx 1/3$ [6] does not change the design conclusion: the NRT-referenced 18.85 is the standard-comparable damage metric that sets the scheduled cadence, while the arc-dpa survival is the physical defect-production rate that the swelling and embrittlement models consume. Because the cadence is anchored to the wall neutron loading through the near-linear proportionality $\kappa_{\mathrm{dpa}} \simeq 10\,\mathrm{dpa\,MW^{-1}\,m^2\,fpy^{-1}}$ (equation 11), it is a simple, auditable function of the operating point rather than a sensitive model output, and it moves predictably with P_{fus} across the ST design box. This is the right kind of limit to have: a scheduled maintenance interval sized by a first-principles damage calculation, feeding the first-wall remaining-useful-life monitor and the centrepost prognostics of the companion papers [33,28].

EROSION, REDEPOSITION AND THE EDGE-ENERGY LEVER

The 0.1–$0.3\,\mathrm{mm\,yr^{-1}}$ recession is manageable precisely because the negative-triangularity edge holds the impact energy below the steep part of the Bohdansky curve (figure 5); above threshold the yield rises as $[1-(E_{\mathrm{th}}/E)^{2/3}](1-E_{\mathrm{th}}/E)^2$, so a modest rise in edge energy would matter. Net erosion is further mitigated by prompt local redeposition, treated quantitatively in the companion plasma–material-interaction study [29]; the gross-recession figure here is therefore a conservative bound. This is consistent with the erosion/redeposition framing of Federici *et al.* [14] for next-step devices.

LEGIBILITY OF THE LIFETIME CASE

The most useful property of the result is not any single margin but its *legibility*: the mechanical and materials modes each carry a comfortable, separately verifiable margin, so none of them is the thing that ends a wall's life, and the design driver collapses to a single well-understood mechanism whose consequence is a plannable interval. For a first-of-a-kind nuclear system this converts an open failure-risk question into a scheduled-maintenance line item.

§ 6

Limitations

One honest gate bounds the swelling claim. The helium-swelling values of equations (13)–(15) are computed with a reduced zero-dimensional rate-theory model closed by the van der Waals equation of state; the confirming calculation is a high-fidelity cluster-dynamics arbiter (Xolotl-class) that resolves the full bubble-size distribution and its temperature dependence, which is routed to the HPC campaign as the follow-on. The reduced model and the independent kinetic-Monte-Carlo corroboration agree on nanometre bubbles and sub-percent swelling (BR-L2-A26), so the design conclusion is not expected to move; but the sub-percent number should be read as reduced-model-plus-KMC until the cluster-dynamics arbiter closes it. The reported temperature profile (figure 3) is likewise a one-dimensional reduction whose peak value is pinned to the two-dimensional CHT anchor; a full three-dimensional thermomechanical pass on the as-built vacuum-vessel heat path is the natural next step.

§ 7

Conclusion

At the frozen Hyperion design point ($P_{\text{fus}} = 85.04$ MW, $\Gamma_{\text{w}} = 1.885$, $\delta = -0.30$) the first wall carries margin in every mechanical and materials mode. Solving each governing problem on the NVIDIA GPU HPC campaign gives helium swelling of $0.024\,\%$/fpy against a 1–$5\,\%$ tolerance, Palmgren–Miner fatigue damage of 3×10^{-6}, a demount-joint life $5434\times$ its 200-mate duty, a RAFM structural temperature of 516 with 34 to spare, and 0.1–0.3 mm yr^{-1} erosion at the nominal sub-500 eV edge. The single argument of the lifetime minimisation (21) that binds is bulk neutron displacement damage at 18.85 , which the machine handles as a scheduled-replacement cadence sized by a first-principles calculation. The plasma-facing-component lifetime case for a compact spherical-tokamak breeder is therefore thermomechanically comfortable and damage-limited by design.

Acknowledgments tocsectionAcknowledgments Part of the Kronos Fusion Energy 2026 design series. The authors thank the Kronos physics de-risking programme for the frozen result set underlying every quantitative claim.

Reproducibility. The damage, fatigue, swelling and thermal-margin values are frozen results (BR-L1-A13, BR-L1-A13b, QS-12, BR-L2-A24, BR-L2-A26, BR-SX-15, AG-CX-27, BV-04) in the Kronos Physics De-Risking Register, the register is doi:10.5281/zenodo.22133057; displacement damage is regenerable from the OpenMC depletion and LAMMPS cascade archives, and the figure-generation script is deposited with this paper. This paper is archived at its DOI doi:10.5281/zenodo.22645850 and its official page https://www.kronosfusionenergy.com/publications/first-wall-thermomechanics-and-fatigue-life-of-plasma-f.html.

Data availability tocsectionData availability This paper is archived at doi:10.5281/zenodo.22645850. Damage, thermal, swelling and fatigue inputs and the figure scripts are archived with the deposit and reference the Kronos 2026 series and its Physics De-Risking Register (doi:10.5281/zenodo.22133057). Any economic analysis is reported separately and is not included in the public deposit.

Competing interests tocsectionCompeting interests Provisional patent applications relating to aspects of this work have been filed.

tocsectionReferences

APPARATUS

Portfolio, People & Record

The intellectual-property estate, the people who built it, the limitations that gate it, and the sources it rests on.

1	4	40	27
GRANTED PATENT	2026 PROVISIONALS	TEAM MEMBERS	2022 PROVISIONALS

INTELLECTUAL PROPERTY

The patent portfolio

The estate spans a granted high-field magnet patent, pending utility and 2026 provisional filings that map to the two products, a digital-twin control provisional, a registered trademark application, and the original 2022 provisional family. Every patentable disclosure in the five-paper arXiv drop was protected **before** publication: the breeder and burner provisionals were filed 1–2 August, and a publication-gap omnibus filing the evening before the drop swept up the DEC, plasma-control, and REBCO-winding matter of the three otherwise-unprotected papers. Patent numbers and application serials are matters of public record; claim scope is summarised, not reproduced.

GRANTED & PENDING UTILITY

US 12,009,112	High-field tilted graded-REBCO magnet architecture (KRONO-002A) · *app. 17/878,550*	GRANTED
US 17/878,507	Core device / method (KRONO-001A) · *utility*	PENDING

2026 PROVISIONAL FILINGS — MAPPED TO THE PRODUCTS

64/124,209	Hyperion — spherical-tokamak tritium / helium-3 foundry · *breeder · filed Aug 2026*	FILED
64/124,220	Aegis / MetroVolt — synchrotron-cutoff, fuel-selection & plug-winding · *generator · filed Aug 2026*	FILED
64/115,167	KRONOS-CTRL digital-twin plant control · *provisional · filed Jul 2026*	FILED
64/005,440	Integrated spherical-tokamak fusion architecture · *early integrated-architecture filing · filed Mar 2026*	FILED
64/105,530	Negative-triangularity spherical-tokamak architecture · *foundational ST filing · filed Jul 2026*	FILED
64/128,097	Publication-gap omnibus — quasineutral two-species expander DEC · provenance-gated / latency-split plasma control · as-built high-field winding & conductor architecture · *filed 7 Aug 2026, the evening before the arXiv drop*	FILED

TRADEMARK & ORIGIN

FTK-98801894	Kronos Fusion Energy — trademark application	FILED
KR-2022-*	Original provisional family (KR-2022-00001 … 00027) · *27 filings, 2022*	PRIORITY

The narrow, defensible magnet novelty — the specific conductor and the digital-twin winding optimisation, not high-field REBCO as a category — is the commercial core that can earn ahead of any Q > 1 milestone, with markets in fusion magnet supply, MRI/NMR, accelerators, and proton therapy. The claim is scoped honestly: the high field is a *system field* result, not a stand-alone-coil record; the small-bore plug coil is structurally infeasible as a bare winding but resolved by a stress-managed structural shield (feasible-pending-FEA); and the winding-tape experiment returned a *null result*. The value is the method, not a field record.

THE TEAM

Founding partners, board, advisors & auditors

Kronos is built by a bench of advanced-fuel-fusion, high-field-magnet, direct-conversion, and materials specialists, with a board and operations team drawn from defense, national laboratories, and industry. Dates are shown as ranges; where a tenure has ended or is term-ending, the range says so.

FOUNDING PARTNERS — SCIENCE

Dr. Gerald Kulcinski
Co-Founder · Helium-3 & Advanced-Fuel Fusion
UW–Madison · 2023–Present

Dr. Carl Weggel
Chief Scientist / S.M.A.R.T. Design
MIT Alcator Program · 2022–Present

Dr. Robert J. Weggel
Magnetic Field Design
MIT Magnet Lab · 2022–Present

BOARD

Priyanca Ford
Founder & CEO · Executive Board
2022–Present

Bandel Carano
Finance / Strategy
Oak Investment Partners / Stanford · 2025–2026

Patrick Schweiger
Fusion Device Engineering
Oklo / CFS / TerraPower · 2025–Present

SCIENTIFIC ADVISORS

Dr. Steven O. Dean
Fusion Policy & History
DOE / Fusion Power Associates · 2025–Present

Dr. Patrick H. Diamond
Plasma Turbulence & Transport
UC San Diego · 2025–Present

Dr. Jack J. Dongarra
HPC & Numerical Algorithms
Turing Award · 2025–Present

Dr. Nasr M. Ghoniem
Chief Material Scientist
UCLA · 2025–Present

Dr. Siegfried Glenzer
Plasma Physics & Laser Fusion
Stanford / SLAC · 2022–Present

Dr. David A. Hammer
Pulsed-Power Fusion
Cornell · 2025–Present

Dr. Donald A. Spong
Plasma Theory & Confinement
ORNL · 2025–Present

Dr. Curtis Smith
Risk Assessment & Nuclear PRA
MIT / Idaho National Lab · 2025–Present

RADM (Ret.) David Goggins
Naval Engineering & Power-Plant Design
U.S. Navy · 2023–2026

Dr. Konstantin Batygin
Mathematician
Caltech · 2022–2025

Dr. Ruben Fair
Magnet Design / ITER Liaison
PPPL / Jefferson Lab · 2022–2025

Dr. Paul S. Weiss
Materials & Nanotechnology
UCLA · 2022–2025

SCIENTIFIC AUDITORS

Dr. Wilfred A. Cooper
Plasma Equilibrium Theory
EPFL / Swiss Plasma Center · 2025–Present

Dr. Ahmed Hassanein
Plasma–Material Interactions
Purdue / Argonne · 2025–Present

Dr. Patrick E. Hopkins
Extreme Thermal Materials
U. of Virginia · 2025–Present

Dr. Peter Hosemann
Materials Joining & Structural Integrity
UC Berkeley · 2025–Present

Dr. Travis W. Knight
Advanced Nuclear Fuels & Systems
U. of South Carolina · 2025–Present

Dr. Philippe Lebrun
Cryogenics & Magnet Cooling
CERN · 2025–Present

Dr. Nitendra Singh
Nuclear Safety & Fuel Cycle
ITER · 2025–Present

Dr. Guido Van Oost
Magnetic Confinement & Fusion Systems
Ghent University · 2025–Present

Dr. Gary S. Was
Radiation Materials & Structural Integrity
U. of Michigan · 2025–Present

Dr. Ray Sedwick
Direct Energy Conversion
U. of Maryland · 2025

OPERATIONS

Michael Laughlin
Chief Operating Officer
2022–Present

Martin Owens
Chief Strategy Officer
LANL / GE Hitachi · 2022–Present

MG (Ret.) Paul Pardew
Chief Contracting Officer
Army Contracting Command · 2022–Present

David Beck
Fusion Commercialization
U.S. Space Force · 2024–Present

Sushma Bhatia
Environmental & Legislative
Google · 2022–Present

Michael De Frenza
Technology Licensing
2023–Present

MG (Ret.) Robin L. Fontes
Cybersecurity & Defense
Army Cyber Command · 2022–Present

Vijay Gehani
Supply Chain & Components
INOX India · 2024–Present

Jon Michel Greenwood
IT & AI Infrastructure
Live Nation · 2023–Present

Brian C. O'Neill
National Security
CIA / ODNI · 2022–Present

Gen. (Ret.) Gustave F. Perna
DoD Liaison
Operation Warp Speed · 2022–2023

Andrea Romero
Marketing Lead
2022–Present

Legal counsel is retained; those roles are held on the internal roster and are not listed here.

SOURCES

References

1 J E Menard *et al*, Fusion nuclear science facilities and pilot plants based on the spherical tokamak, *Nucl. Fusion* **56** 106023 (2016). doi:10.1088/0029-5515/56/10/106023

2 B N Sorbom *et al*, ARC: a compact, high-field, fusion nuclear science facility and demonstration power plant with demountable magnets, *Fusion Eng. Des.* **100** 378 (2015). doi:10.1016/j.fusengdes.2015.07.008

3 M E Austin *et al*, Achievement of reactor-relevant performance in negative triangularity shape in the DIII-D tokamak, *Phys. Rev. Lett.* **122** 115001 (2019). doi:10.1103/PhysRevLett.122.115001

4 A Marinoni, O Sauter and S Coda, A brief history of negative triangularity tokamak plasmas, *Rev. Mod. Plasma Phys.* **5** 6 (2021). doi:10.1007/s41614-021-00054-0

5 M J Norgett, M T Robinson and I M Torrens, A proposed method of calculating displacement dose rates, *Nucl. Eng. Des.* **33** 50 (1975). doi:10.1016/0029-5493(75)90035-7

6 K Nordlund *et al*, Improving atomic displacement and replacement calculations with physically realistic damage models, *Nat. Commun.* **9** 1084 (2018). doi:10.1038/s41467-018-03415-5

7 S J Zinkle and N M Ghoniem, Operating temperature windows for fusion reactor structural materials, *Fusion Eng. Des.* **51–52** 55 (2000). doi:10.1016/S0920-3796(00)00320-3

8 R Lindau *et al*, Present development status of EUROFER and ODS-EUROFER for application in blanket concepts, *Fusion Eng. Des.* **75–79** 989 (2005). doi:10.1016/j.fusengdes.2005.06.186

9 M Rieth *et al*, Recent progress in research on tungsten materials for nuclear fusion applications in Europe, *J. Nucl. Mater.* **432** 482 (2013). doi:10.1016/j.jnucmat.2012.08.018

10 M R Gilbert and J-Ch Sublet, Neutron-induced transmutation effects in W and W-alloys in a fusion environment, *Nucl. Fusion* **51** 043005 (2011). doi:10.1088/0029-5515/51/4/043005

11 H Trinkaus and B N Singh, Helium accumulation in metals during irradiation — where do we stand?, *J. Nucl. Mater.* **323** 229 (2003). doi:10.1016/j.jnucmat.2003.09.001

12 S J Zinkle and L L Snead, Designing radiation resistance in materials for fusion energy, *Annu. Rev. Mater. Res.* **44** 241 (2014). doi:10.1146/annurev-matsci-070813-113627

13 G R Odette, M J Alinger and B D Wirth, Recent developments in irradiation-resistant steels, *Annu. Rev. Mater. Res.* **38** 471 (2008). doi:10.1146/annurev.matsci.38.060407.130315

14 G Federici *et al*, Plasma-material interactions in current tokamaks and their implications for next step fusion reactors, *Nucl. Fusion* **41** 1967 (2001). doi:10.1088/0029-5515/41/12/218

15 J Bohdansky, A universal relation for the sputtering yield of monatomic solids at normal ion incidence, *Nucl. Instrum. Methods B* **2** 587 (1984). doi:10.1016/0168-583X(84)90271-4

16 M A Miner, Cumulative damage in fatigue, *J. Appl. Mech.* **12** A159 (1945). doi:10.1115/1.4009458

17 P K Romano *et al*, OpenMC: a state-of-the-art Monte Carlo code for research and development, *Ann. Nucl. Energy* **82** 90 (2015). doi:10.1016/j.anucene.2014.07.048

18 D A Brown *et al*, ENDF/B-VIII.0: the 8th major release of the nuclear reaction data library with CIELO-project cross sections, new standards and thermal scattering data, *Nucl. Data Sheets* **148** 1 (2018). doi:10.1016/j.nds.2018.02.001

19 A P Thompson *et al*, LAMMPS — a flexible simulation tool for particle-based materials modeling at the atomic, meso, and continuum scales, *Comput. Phys. Commun.* **271** 108171 (2022). doi:10.1016/j.cpc.2021.108171

20 J T Drobny and D Curreli, RustBCA: a high-performance binary-collision-approximation code for ion-material interactions, *J. Open Source Softw.* **6** 3298 (2021). doi:10.21105/joss.03298

21 S P Timoshenko and J N Goodier, *Theory of Elasticity*, 3rd edn (McGraw-Hill, New York, 1970).

22 B A Boley and J H Weiner, *Theory of Thermal Stresses* (Wiley, New York, 1960).

23 H S Carslaw and J C Jaeger, *Conduction of Heat in Solids*, 2nd edn (Oxford University Press, Oxford, 1959).

24 G S Was, *Fundamentals of Radiation Materials Science: Metals and Alloys*, 2nd edn (Springer, New York, 2017).

25 O C Zienkiewicz, R L Taylor and J Z Zhu, *The Finite Element Method: Its Basis and Fundamentals*, 7th edn (Butterworth-Heinemann, Oxford, 2013).

26 S Suresh, *Fatigue of Materials*, 2nd edn (Cambridge University Press, Cambridge, 1998).

27 P I Ford, *Kronos Physics De-Risking Register*, Kronos Fusion Energy 2026 series. doi:10.5281/zenodo.22133057

28 P I Ford, First-wall and plasma-facing-component lifetime under 14 MeV loading: displacement damage, bubble swelling and erosion in a compact spherical-tokamak breeder, Kronos 2026 series. doi:10.5281/zenodo.22645774; https://www.kronosfusionenergy.com/publications/first-wall-neutron-damage-lifetime.html

29 P I Ford, Plasma-material interaction in a compact spherical-tokamak breeder: sputtering, net erosion, and redeposition setting the plasma-facing-surface lifetime, Kronos 2026 series. doi:10.5281/zenodo.22645885; https://www.kronosfusionenergy.com/publications/plasma-material-interaction-in-a-compact-spherical-toka.html

30 P I Ford, Blanket and divertor thermal-hydraulics for a compact spherical-tokamak breeder: coolant heat removal, peak-temperature margins, and the walk-away safety case, Kronos 2026 series. doi:10.5281/zenodo.22645836; https://www.kronosfusionenergy.com/publications/blanket-and-divertor-thermal-hydraulics-for-a-compact-s.html

31 P I Ford, Qualifying reduced-activation ferritic-martensitic steel for a compact spherical-tokamak breeder: strength, DBTT shift and swelling under 14 MeV neutron loading, Kronos 2026 series. doi:10.5281/zenodo.22645887; https://www.kronosfusionenergy.com/publications/qualifying-reduced-activation-ferritic-martensitic-stee.html

32 P I Ford, The centrepost life-limiter: fast-fluence, dpa, and shielding setting the cartridge-replacement cadence for a compact spherical-tokamak breeder, Kronos 2026 series. doi:10.5281/zenodo.22645708; https://www.kronosfusionenergy.com/publications/centrepost-fluence-and-shielding.html

33 P I Ford, Prognostics and remaining-useful-life estimation for the consumable centrepost, Kronos 2026 series. doi:10.5281/zenodo.22645788; https://www.kronosfusionenergy.com/publications/centrepost-prognostics-and-rul-control.html

34 P I Ford, Negative-triangularity turbulence suppression in a compact spherical-tokamak breeder: nonlinear gyrokinetics of ion- and electron-scale quiescence at the operating point, Kronos 2026 series. doi:10.5281/zenodo.22645722; https://www.kronosfusionenergy.com/publications/negative-triangularity-confinement.html

35 P I Ford, Component activation, waste-class routing, and decommissioning of a low-activation compact spherical-tokamak breeder, Kronos 2026 series. doi:10.5281/zenodo.22645846; https://www.kronosfusionenergy.com/publications/component-activation-waste-class-routing-and-decommissi.html

COLOPHON

How this document was made

The Kronos Fleet — Combined Editorial, 2026 is set in **Fraunces** (display), **Gelasio** (text), and **IBM Plex Mono** (data & equations), carried forward from the Kronos editorial design system.

The figures are rendered at 300 dpi from the deposited generator scripts; the document is composed as a single self-contained file with embedded fonts and imagery, paginated to US Letter, and rendered to PDF through a headless Chromium engine in matched light and dark editions.

Every headline quantity carries an evidence class; withdrawn and restated values are marked as such. Nothing herein is frozen beyond the founder-approved Tier-A set.

Explore it live — turn the interactive 3-D model, run the deposited solvers in the physics validator, and watch the companion film series.

LEGAL NOTICE

Notice, status, and distribution

Conceptual design & simulation study. This document reports a conceptual design and simulation study. It is not a construction commitment, a safety-analysis report, a regulatory filing, or an offer of securities. Forward-looking statements — schedules, costs, market sizes, and performance — are estimates subject to the limitations set out in the Simulations part and may change.

Numbers and their classes. Quantities are reported with evidence classes and case labels; modelled, assumed, and requirement-class values are identified as such and are not to be quoted without their labels.

Public edition. This edition carries the physics and design only; all financial, funding, and defense-commercial content has been removed for public distribution. The scientific text corresponds to the arXiv and journal submissions.

THE 2026 KRONOS SERIES

One programme, many papers

This editorial is one paper in the Kronos 2026 series — a real fusion company's complete, reproducible physics record for a spherical-tokamak breeder and its low-neutron D–^{3}He tandem-mirror burners. Every headline number is a frozen anchor in the Physics De-Risking Register.

Explore the whole programme: the De-Risking Register, the interactive 3-D model, and the physics validator.

KRONOS FUSION ENERGY

First-Wall Thermomechanics and Fatigue Life of Plasma-Facing Components Under Combined Surface and Volumetric Loading in a Compact Spherical-Tokamak Breeder

A real fusion company building real machines. Explore the science, live.

Zenodo · doi:10.5281/zenodo.22645850

Read on kronosfusionenergy.com

The Physics De-Risking Register